

Lateral-Polarity Structure of AlGa_N Quantum Wells: A Promising Approach to Enhancing the Ultraviolet Luminescence

Wei Guo, Haiding Sun, Bruno Torre, Junmei Li, Moheb Sheikhi, Jiean Jiang, Hongwei Li, Shiping Guo, Kuang-Hui Li, Ronghui Lin, Andrea Giugni, Enzo Di Fabrizio, Xiaohang Li,* and Jichun Ye*

Aluminum-gallium-nitride alloys (Al_xGa_{1-x}N, 0 ≤ x ≤ 1) can emit light covering the ultraviolet spectrum from 210 to 360 nm. However, these emitters have not fulfilled their full promise to replace the toxic and fragile mercury UV lamps due to their low efficiencies. This study demonstrates a promising approach to enhancing the luminescence efficiency of AlGa_N multiple quantum wells (MQWs) via the introduction of a lateral-polarity structure (LPS) comprising both III and N-polar domains. The enhanced luminescence in LPS is attributed to the surface roughening, and compositional inhomogeneities in the N-polar domain. The space-resolved internal quantum efficiency (IQE) mapping shows a higher relative IQE in N-polar domains and near inversion domain boundaries, providing strong evidence of enhanced radiative recombination efficiency in the LPS. These experimental observations are in good agreement with the theoretical calculations, where both lateral and vertical band diagrams are investigated. This work suggests that the introduction of the LPS in AlGa_N-based MQWs can provide unprecedented tunability in achieving higher luminescence performance in the development of solid state light sources.

The Al_xGa_{1-x}N (0 ≤ x ≤ 1) alloy has tunable and direct band gap ranging from 3.4 to 6.1 eV that covers the UV spectral region from 360 to 210 nm,^[2] which are particularly suitable for the UV LEDs.^[3] However, the UV-LED performance has not yet reached the level obtained in highly commercialized InGa_N-based blue counterparts.^[4] The best-performing UV LEDs have been grown on the III-polar (0001) structure so far.^[1a] Nevertheless, the usage of N-polar (000 $\bar{1}$) nitride films has also gained attentions recently due to their distinct advantages such as reduced efficiency droop in the application of LEDs,^[5] enhanced electrical field distribution in *p-i-n* diodes,^[6] and susceptibility to wet etching,^[7] which can be used for nanostructure fabrication.^[8]

To take full advantage of both III and N-polar domains in the development of high efficiency UV LEDs, the lateral-polarity structure (LPS) can be a promising

candidate owing to its unique structural properties, in which III and N-polar domains are grown simultaneously side by side on the same substrate.^[9] Recently, the LPS has been applied in the application of second harmonic generation^[9b,10] and lateral *p-n* junction MESFET.^[11] Hite, Kirste, and Hoffmann et al. have

1. Introduction

There are growing demands for mercury-free, environmentally friendly, compact ultraviolet (UV) LEDs for crucial applications such as water/air disinfection, biosensing, and epoxy curing.^[1]

Dr. W. Guo, J. Li, M. Sheikhi, J. Jiang, Prof. J. Ye
Ningbo Institute of Materials Technology and Engineering (NIMTE)
Chinese Academy of Sciences
Ningbo 315201, Zhejiang, China
E-mail: jichun.ye@nimte.ac.cn

Dr. W. Guo
Zhejiang Key Laboratory for Advanced Microelectronic
Intelligent Systems and Applications
Hangzhou 310007, Zhejiang, China
Dr. H. Sun, K.-H. Li, R. Lin, Prof. X. Li
Advanced Semiconductor Laboratory
King Abdullah University of Science and Technology (KAUST)
Thuwal 23955-6900, Saudi Arabia
E-mail: xiaohang.li@kaust.edu.sa

Dr. B. Torre, Dr. A. Giugni, Prof. E. D. Fabrizio
Structural Molecular Imaging Light Enhanced Spectroscopies Lab
King Abdullah University of Science and Technology (KAUST)
Thuwal 23955-6900, Saudi Arabia

M. Sheikhi, J. Jiang
University of Chinese Academy of Sciences
No.19(A) Yuquan Road, Shijingshan District, Beijing 100049, P. R. China
H. Li, S. Guo
Advanced Micro-Fabrication Equipment Inc.
Shanghai 201201, China

 The ORCID identification number(s) for the author(s) of this article can be found under <https://doi.org/10.1002/adfm.201802395>.

DOI: 10.1002/adfm.201802395

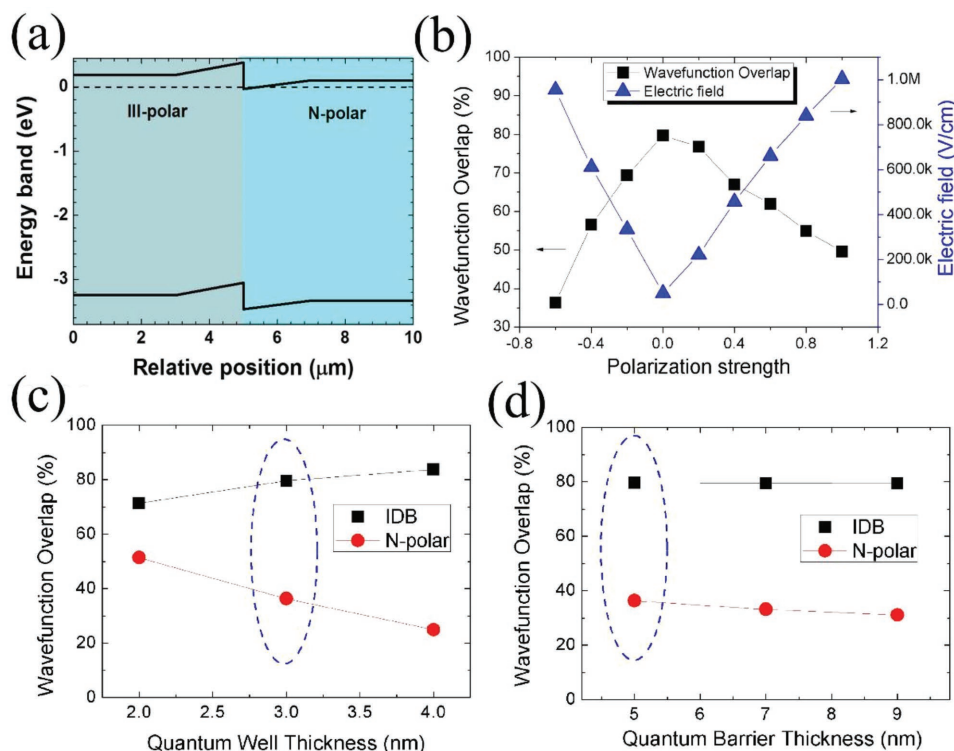


Figure 1. Schematic lateral energy band diagram of the LPS in the vicinity of IDB in thermal equilibrium case. a) The Fermi level is denoted as the horizontal dashed line. b) Influence of polarization strength on carrier wavefunction overlap and electric field inside QWs. Influence of c) QW and d) QB thickness on the carrier wavefunction overlap in N-polar domains as well as in the vicinity of IDB.

successfully synthesized GaN, AlN, and AlGaIn LPS on sapphire substrates.^[9a,c,d] The polarity of the epitaxial nitride films can be controlled by the introduction of a low-temperature (LT) AlN buffer layer. The epitaxial film grown on the LT-AlN buffer exhibits III-polarity, while the one grown on bare sapphire with proper annealing condition shows N-polarity.^[12] Regarding the optical properties, Kirste et al. observed a high photoluminescence (PL) intensity at the boundaries between N and III-polar GaN film due to the localized surface potential difference.^[13] Coulon et al., on the other hand, demonstrated higher near-band-edge luminescence in N-polar regions of randomly distributed GaN micropillars due to unequal impurity incorporations in different domains.^[14] These results indicate that polarity manipulation can be important for formation of desirable film properties amid enhanced luminescence intensity. In spite of these advances, there are yet applications of the LPS in optoelectronics (i.e., LPS-based AlGaIn/GaN multiple quantum wells (MQWs)), especially when the domain size of each polarity is reduced similar to the atom lateral diffusion length of only several micrometers,^[13] in which case a new physical phenomenon may occur. It is noted that a depletion region can be formed by combining III and N-polar thin films side by side due to opposite intrinsic polarization vectors induced by adjacent opposite-polarity regions,^[15] which requires detailed optical and electrical characterization. In this work, we design, grow, and characterize a novel AlGaIn/GaN MQW based on LPS to enhance the luminescence performance. The influence of different polarity domains on the optical behavior such as internal quantum efficiency (IQE) and PL intensity was discussed. Undoubtedly, the approach of

LPS provides advantageous possibility regarding the regulation of luminescence intensity of next-generation UV emitters.

2. Results and Discussions

2.1. Band Diagram and Structure Design

The electron concentrations in pure III and N-polar $\text{Al}_{0.1}\text{Ga}_{0.9}\text{N}$ -GaN MQWs were measured to be $3.6 \times 10^{17} \text{ cm}^{-3}$ and $1.1 \times 10^{18} \text{ cm}^{-3}$ via Hall effect characterization. The discrepancy between these two polarities is due to higher oxygen levels in N-polar domains (see Figure S1 in the Supporting Information). Fermi levels in each domain can be estimated consequently,^[16] and the schematic lateral band diagram of the GaN quantum well (QW) in LPS is shown in Figure 1a. Different carrier concentrations and the opposite sign of the spontaneous polarization of III and N-polar domains lead to a depletion region perpendicular to the interface of the inversion domain boundaries (IDBs) as reported by Fiorentini et al. and Collazo et al.^[15a,17] Electron affinity level for N-polar MQW is higher than III-polar MQWs by 0.51 eV measured from ultraviolet photoelectron spectroscopy. This results in band edge discontinuities that are only localized at the surface.^[18] However, it is noted that since majority of the polarization bound surface charge is screened in the LPS,^[19] IDB was demonstrated not to hinder the lateral carrier transport.^[20]

To quantitatively assess the influence of MQW dimensions and polarization strength on the radiative recombination

efficiency, we calculated the wavefunction overlap and electric field intensities inside QWs utilizing a self-consistent 6-band $k \cdot p$ method.^[21] As shown in Figure 1b, the x -axis indicates the polarization strength (p), which specifies a constant scale factor multiplied by the calculated spontaneous and piezoelectric polarization charges. Pure III-polarity has a positive value, while pure N-polarity shows a negative value. In the vicinity of IDB, a mixture of III and N-polarization is expected, represented by polarization strength $p = 0$.^[22] Obviously, wavefunction overlap reaches its maximum point of 79.7% in the IDB, indicating a more balanced carrier distribution due to relieved quantum-confined stark effect. The electric field is obtained from the gradient of the potentials, and it has an opposite trend with respect to the wavefunction overlap. This can be explained as the separation of electrons and holes on the two sides of the QW, which promotes a strong built-in electric field at larger p magnitude. Figure 1c,d shows the variations of wavefunction overlaps as functions of QW and quantum barrier (QB) thickness, respectively. Two polarization conditions were used, i.e., N-polarity and in the IDB region. In Figure 1c, the QB thickness is fixed at 5 nm. With increasing QW thickness from 2 to 4 nm, wavefunction overlap decreases from 51.4% to 24.9% for N-polarity, suggesting less effective quantum confinement as QW thickness increases. This is in good accordance with reports from Schlichting et al.^[23] However, wavefunction overlap increases slightly from 71.4% to 83.7% with thicker QW thickness in the case of $p = 0$ since the wavefunctions of both electrons and holes are located in the center of the QW due to the absence of the internal electric field. Considering that radiative recombination would occur in both N-polar domains and IDBs, a balance value of 3 nm QW thickness was chosen in this work as annotated by the dashed circle (Figure 1c). Figure 1d shows the change in wavefunction overlap with respect to QB thickness with a constant QW thickness of 3 nm. Only slight degradation of wavefunction overlap was observed.

2.2. Surface Morphology and Atom Arrangements

$\text{Al}_{0.1}\text{Ga}_{0.9}\text{N}/\text{GaN}$ MQWs consisting of sub-micrometer LPS domains was fabricated based on the structural design shown in the previous section. The schematic process flow is illustrated in Figure 2a with the cross-sectional structure shown in Figure 2b. Polarity domain periodicities of 2 and 6 μm were adopted in this work.

Uniform distribution of the round-shaped LT-AlN buffers is observed after reactive ion etching (RIE) patterning as shown by the atomic force microscopy (AFM) images in

Figure 3a,b. Subsequent to the epitaxy, surface morphologies of the LPS are shown by top-view scanning electron microscope (SEM) images in Figure 3c,d. The surface of the circular shape region is atomically smooth (see Figure S2 in the Supporting Information), while the matrix is relatively rough. The KOH selective etching confirms that they are III and N-polar, respectively (see Figure S3 in the Supporting Information).^[7]

Figure 4a displays high-angle annular dark field (HAADF) scanning transmission electron microscopy (STEM) images of the LPS with 2 μm periodicity comprising III and N-polar domains. We observe that the III-polar domains have a smooth surface while N-polar domains consist of V or truncated pyramid shape structures, in line with previous observations of Figure 3. Figure 4c reveals abrupt interfaces between GaN QW and AlGaIn QB. Brighter regions refer to GaN QWs, and darker regions are AlGaIn QBs. The thickness of QW and QB is ≈ 2.8 and 5.2 nm in III-polar domains, consistent with our targeted thickness of 3/5 nm well/barrier. However, the thickness of QW in the N-polar domains varies drastically. The distributions of Al and Ga atoms are highly nonuniform in N-polar domains

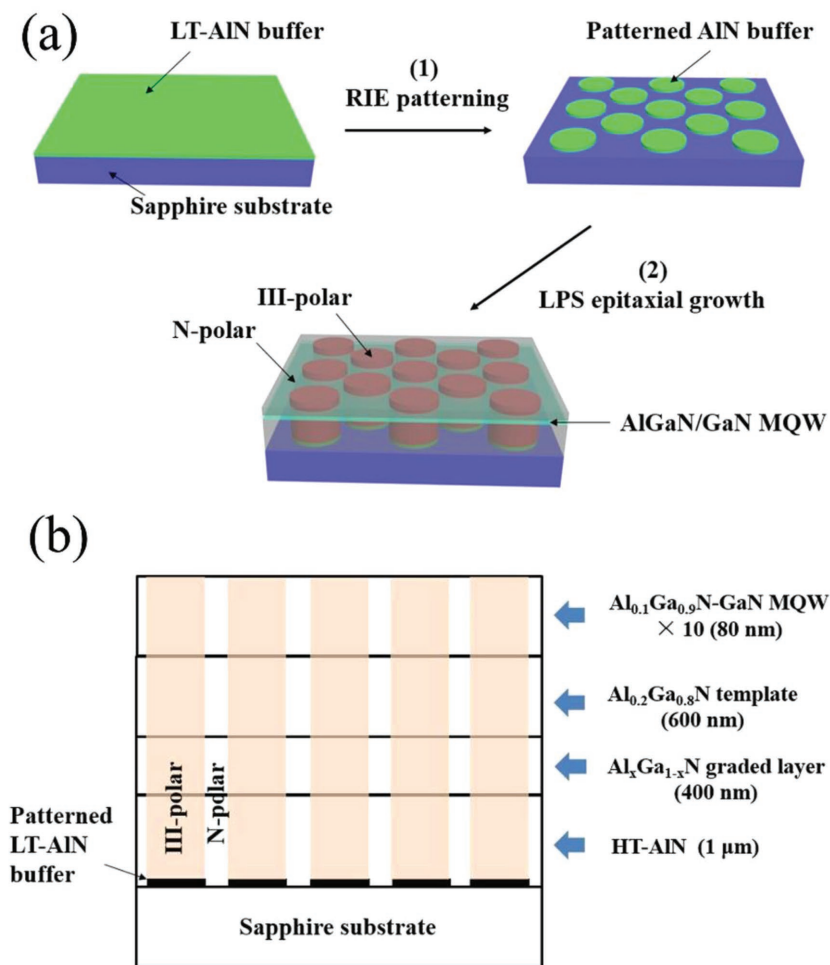


Figure 2. a) Schematic process flow of fabricating the LPS MQW. Step (1) is the selective RIE to achieve patterned LT-AlN buffer. Step (2) is epitaxial growth of the LPS on top of the buffer where red pillars and translucent region represent the III and N-polar domains, respectively. b) Structures of the MQWs with black solid lines representing the buffers; red and white stripes indicate III-polar and N-polar domains, respectively.

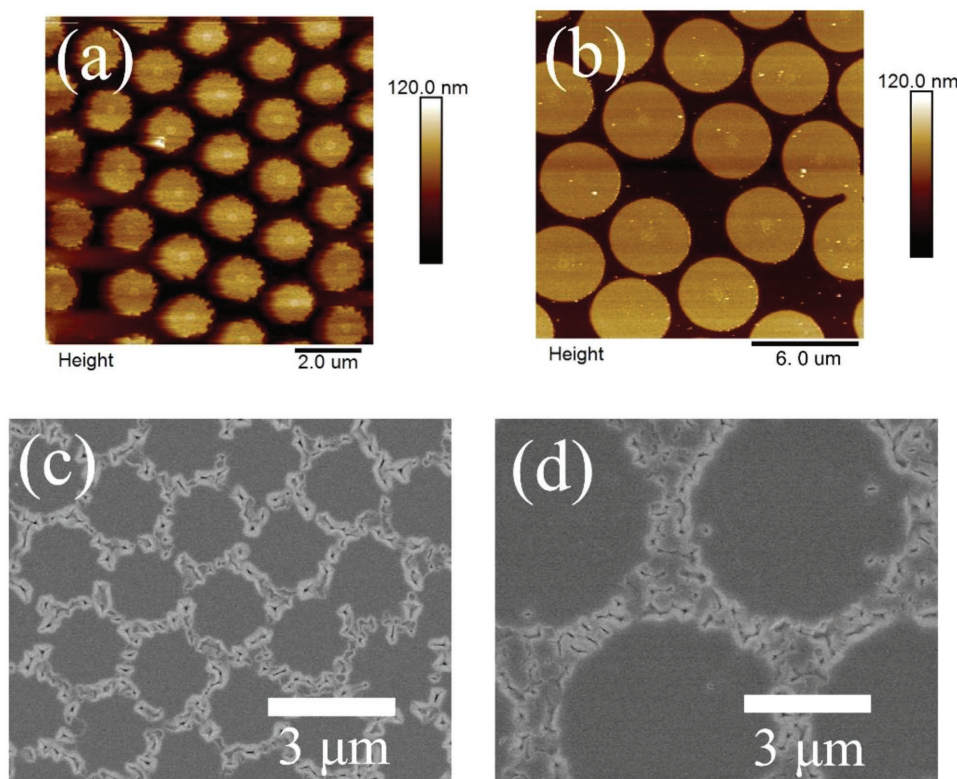


Figure 3. AFM images of the patterned LT-AlN buffers and top-view SEM images of the as-grown LPS MQW with periodicity of a,c) 2 μm and b,d) 6 μm .

by looking at the color contrast (atomic Z-contrast), indicating strong compositional inhomogeneities. Specifically as indicated by the blue dashed circles in Figure 4b, QW and QB do not follow the shape of the N-polar domains, but rather exhibit zigzag features. Another example is shown in Figure S4 of the Supporting Information, where nonuniform QW distributions are observed in the V shape or inverted truncated pyramid shape N-polar domains. Al-rich and Al-deficient regions lead to compositional inhomogeneities, consequently to a stronger carrier localization. In fact, the compositional fluctuation is well known in InGa_N alloy, which is responsible for the high quantum efficiency of blue LEDs.^[24] Moreover, researchers have observed the compositional inhomogeneities in AlGa_N MQWs with enhanced luminescence grown by molecular beam epitaxy (MBE) technique.^[25] To the best of our knowledge, the current study is the first demonstration of metalorganic chemical vapor deposition (MOCVD) grown AlGa_N MQW with composition fluctuations realized through the introduction of sub-micrometer scale LPS.

Finally, polarities of different domains in the LPS were unambiguously identified by atomic resolution STEM illustrated in Figure 4d,e. The vertical bond pointing from the metal atoms to the N atoms defines III-polarity, while bond pointing from opposite direction defines N-polarity.

2.3. Discussion of LPS-MQW Photoluminescence

To study the optical behavior of the LPS-based AlGa_N/Ga_N MQWs, we show the macroscale PL spectra of LPS MQWs

(Figure 5a) with 2 and 6 μm periodicity and that of the pure III-polar AlGa_N/Ga_N MQW (control sample). The dominant emissions of the LPS-MQWs and the pure III-polar MQW are located at around 353 nm, corresponding to an Al composition of 5%,^[26] falling into the targeted Al composition range between Ga_N QW and Al_{0.1}Ga_{0.9}N QB. A substantial increase in the luminescence is observed for LPS, which exceeded the intensity of pure III-polar sample. The enhancement factors of integrated MQW emission intensity for the LPS with 2 and 6 μm periodicity compared to pure III-polar MQW are about 2.1 and 1.3 times, respectively. To explore localized emission characteristics of the LPS MQW samples, micro-PL (μ -PL) mappings were generated from an 8 $\mu\text{m} \times 8 \mu\text{m}$ scanned area for LPS with 2 μm periodicity and a 20 $\mu\text{m} \times 20 \mu\text{m}$ scanned area for LPS with 6 μm periodicity. Integrated intensities of the MQW luminescence were extracted and rendered on Figure 5b,c. The N-polar domains (matrix) show significantly higher PL intensity compared to that of III-polar domains (round islands) with average intensity enhancement greater than 100%. In some regions, PL intensity enhancement as large as six times can be obtained. PL intensity is higher for LPS with 2 μm periodicity than that with 6 μm periodicity, which is consistent with the fact that the area percentage of N-polar domains in LPS with 2 μm periodicity (30.6%) is higher than that in LPS with 6 μm periodicity (18.9%). According to reports from Schuck et al., IDBs are optically active traps, acting as radiative recombination centers, and can lead to enhanced luminescence.^[27] The higher the percentage, the higher the PL intensity. A larger density of IDBs can lead to higher luminescence intensity. Similarly, Kirste et al. reported

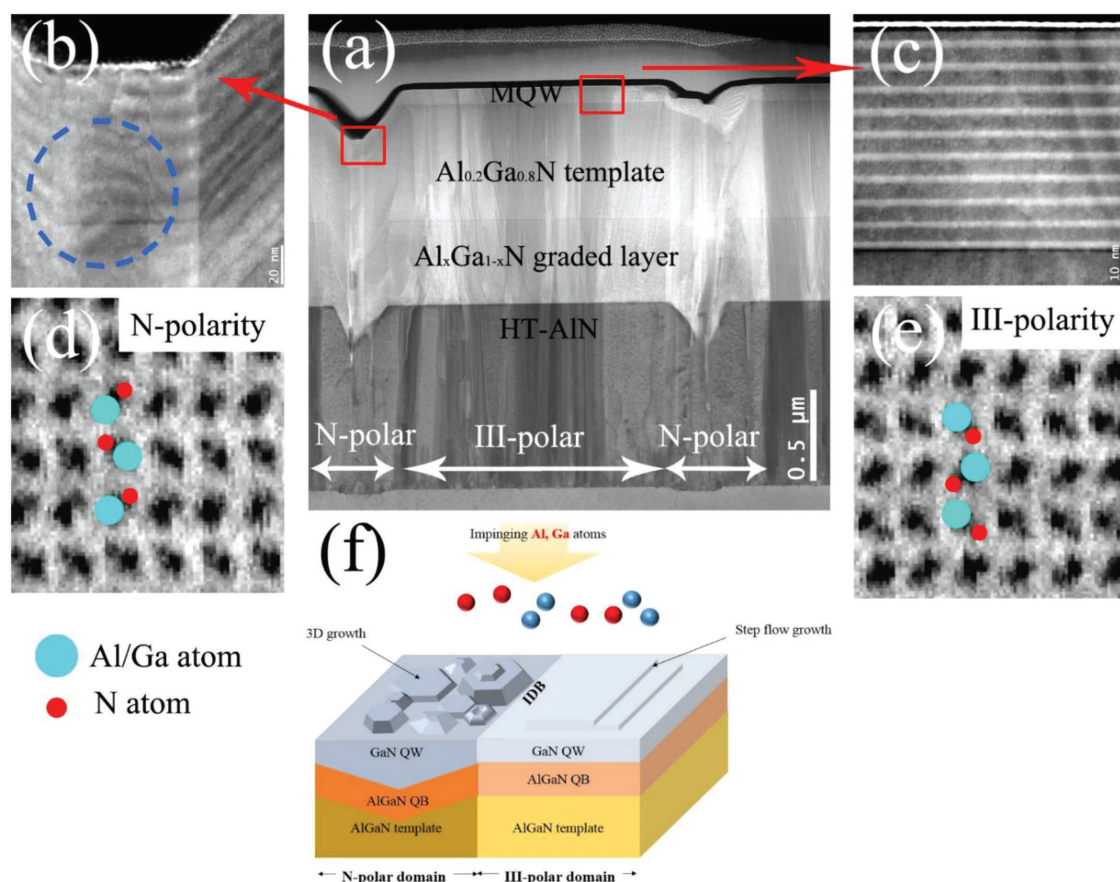


Figure 4. a) The HAADF-STEM cross-sectional image of the sample with 2 μm periodicity. Panels (b) and (c) are high magnification views of MQWs in both N and III-polar domains from the red squares marked in (a). Note that the MQWs have wiggling interfaces in the N-polar domains whereas the interfaces are sharp in the III-polar domains. Atomic resolution STEM images in d) the N-polar e) and III-polar domains. f) Schematic of an LPS near an IDB, illustrating different surface morphologies.

enhanced near-band-edge luminescence in the vicinity of the domain boundaries in a GaN LPS. The strong emission at the IDBs was attributed to the local potential extremes near IDBs,^[13] which can effectively collect carriers for higher radiative recombination. By leveraging such advantage in the IDBs, we are intended to create LPS with optimized coverage and size to enhance the overall luminescence intensity. PL intensity distributions shown in Figure 5b,c are complemented by the space-resolved peak position mapping (see Figure S5 in the Supporting Information). The peak positions of the PL spectra remain nearly identical for LPS with 2 and 6 μm periodicity, suggesting a lack of correlations with the polarity of the film.

To gain further insights into the mechanism of luminescence enhancement in the LPS, a temperature-dependent IQE measurement was adopted. Relative IQE was calculated by $I_{\text{RT}}/I_{\text{LT}}$, where I_{RT} and I_{LT} represent PL intensities at room temperature (RT) and low temperature (LT), respectively.^[3b,28] Due to lacking of liquid helium to reach a temperature of <10 K, I_{LT} was measured at 77 K with liquid N_2 .^[29] LPS was first cooled to 77 K and a low-temperature PL mapping was recorded. Without changing the locations of the sample, the temperature was increased to RT, and a PL mapping was collected again. By taking ratios between I_{RT} and I_{LT} at each position of the 10 $\mu\text{m} \times 10 \mu\text{m}$ scanned area with a lateral resolution of 800 nm, relative IQE distribution of

the LPS with 6 μm periodicity was achieved and is presented in Figure 5e. Since the relative increase of PL intensity becomes slower and further saturates at the temperature below 77 K,^[30] we can use $I_{\text{RT}}/I_{\text{LT}}$ to estimate the radiative recombination efficiency in the LPS roughly. It is observed from Figure 5e that the relative IQE in N-polar domains and at the IDBs are higher than that of in III-polar domains. Furthermore, we found that the IQE of the LPS is estimated to be 58.2% in average, also higher than the IQEs from pure III and N-polar MQWs (they are estimated to be 42% and 29%, respectively), demonstrating that polarity domain itself is unlikely the only reason accounting for the large enhancement of luminescence in the LPS. The IDBs should play a critical role in realizing lateral carrier confinement and thus enhanced radiative recombination.

Another possible reason that accounts for enhanced luminescence intensity in LPS may originate from the V shape or inverted truncated pyramid morphology in N-polar domains due to light scattering. A 2D finite-difference time-domain (FDTD) numerical simulation is carried out to calculate the light extraction efficiency (LEE) of AlGaIn MQWs with and without LPS. The results are shown in Figure S6 in the Supporting Information; the V or truncated pyramid shaped N-polar region indeed introduces light scattering to the otherwise flat region hence the LEE is increased from 9.4% to 11.1% due to local

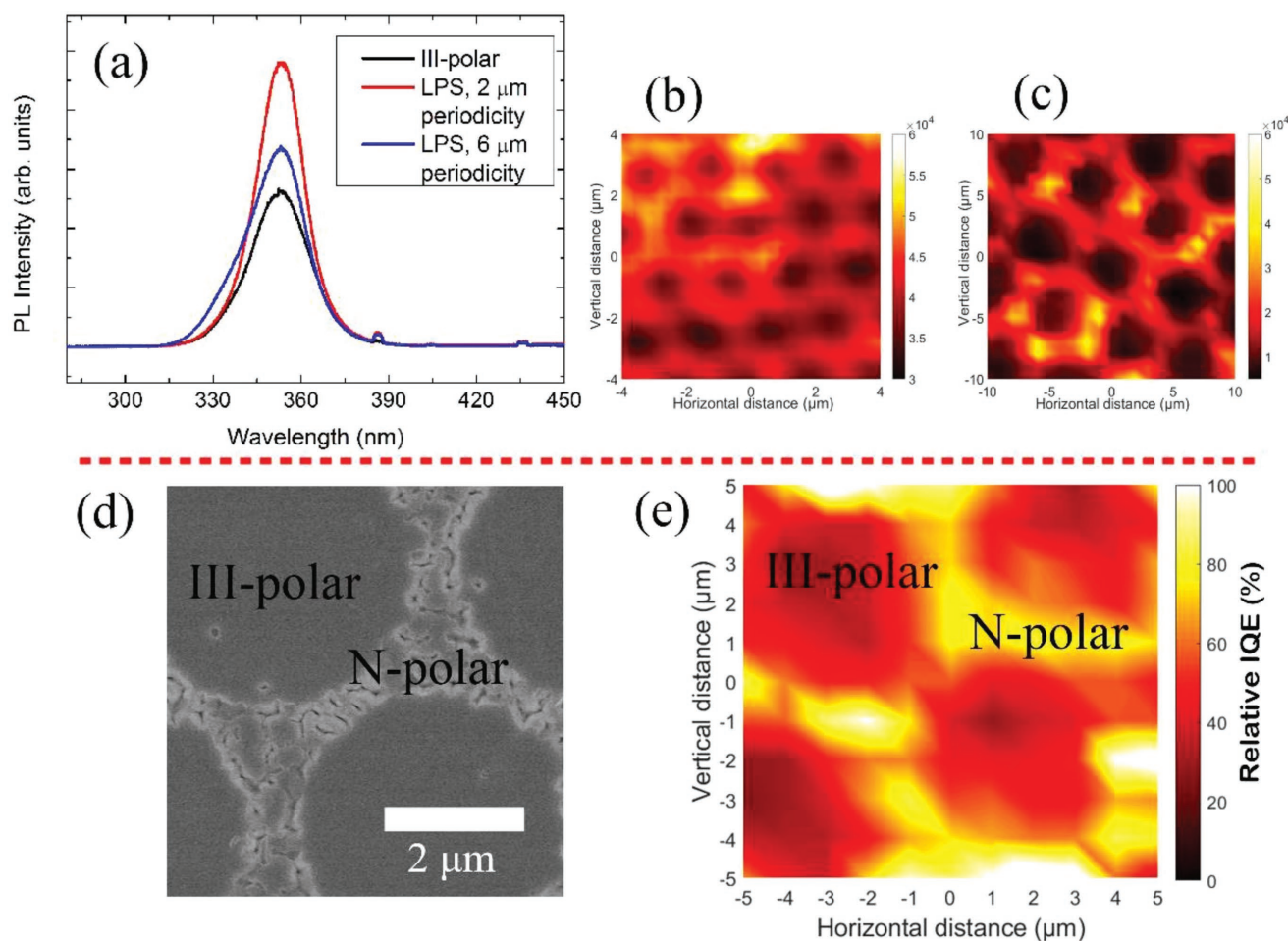


Figure 5. a) PL spectra of the LPS MQWs and pure III-polar MQW. The small peak located at 386 nm is from the second harmonic of 193 nm Ar-F laser. Space-resolved PL intensity mapping of the LPS samples with periodicity of b) 2 μm and c) 6 μm . Color bar represents the integrated emission intensity from the MQWs. Top-view SEM image of the LPS with d) 6 μm periodicity and e) space-resolved relative IQE distributions at the same position as the SEM image.

modification of the field distribution. A moderate LEE enhancement of 18.1% in the LPS MQWs compared with the flat one was obtained. This value is nevertheless relatively smaller than the PL enhancement factor obtained from Figure 5. Thus, we believe a significant contribution of the enhanced PL comes from the improved radiative recombination efficiency in the LPS as shown in Figure 5e.

For a fair comparison, pure III and N-polar MQWs (reference samples) were also subjected to the X-ray diffraction (XRD) and SEM characterizations, and the results were compared with that of the LPS. Figure S7a (Supporting Information) shows the symmetric (002) XRD rocking curve scans of the MQW from pure III-polar, N-polar, and LPS with 2 μm periodicity. Full width at half maximum (FWHM) values are 601, 783, and 571 arcs, respectively. From the equation reported in ref. [31] the threading dislocation (TD) densities in pure III and N-polar MQWs are determined to be $7.86 \times 10^8 \text{ cm}^{-2}$ and $1.33 \times 10^9 \text{ cm}^{-2}$, and the LPS shows a slightly lower density of $7.10 \times 10^8 \text{ cm}^{-2}$. A reduced TD density is commonly observed in the nitrides films grown on a patterned sapphire substrate (PSS), which can effectively reduce the formation of

dislocations. It has been widely reported that the PSS technique improves the IQE.^[32] The technique used in this work not only introduces a unique structure of LPS but also reduces TD thus improve both luminescence intensity and crystalline quality. Still, it is quite difficult to have a direct comparison of TD density in the LPS because the area of N-polar region is limited and thus the density of TD could be highly position-dependent under TEM-based nanoscale investigation. Additionally, Figure S7b,c (Supporting Information) shows the SEM images of pure III and N-polar MQWs. The surface of III-polar MQW is much smoother than that of N-polar one, indicating the dramatically different growth modes between these two films.^[6]

2.4. Surface Potential and Carrier Distributions

As has been mentioned above, compositional inhomogeneities in N-polar domains contribute to the enhancement of PL intensity of the LPS MQW. Moreover, there are significant differences of the spontaneous and piezoelectric polarization in N and III-polar domains,^[33] which could have profound impact

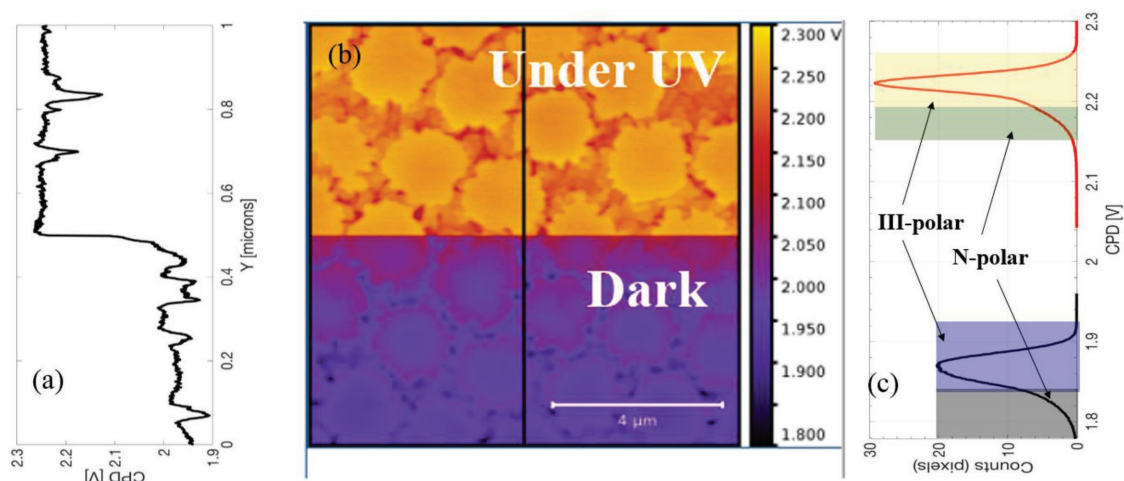


Figure 6. a) Surface potential line scan across the UV/dark region, corresponding to the black line in map (b). b) SKPM surface potential images of the LPS in dark condition and under above band gap UV illumination (image dimensions $3.7 \times 3.7 \mu\text{m}^2$); III and N-polar domains are easily recognized under both illumination conditions by a constant potential difference of ≈ 0.1 V. c) Statistical distribution of the CPD values under dark and UV conditions: colored rectangles highlight the most significant CPD values in III and N-polar domains, corresponding to similar color in map (b).

on the internal electrical field as well as the band alignment, leading to the uneven distribution of the photon-generated carriers at the LPS, as indicated in Figure 1. To further verify this idea, carrier distribution within the LPS is characterized at the nanoscale by Scanning Kelvin Probe Microscopy (SKPM) technique.^[34] Specifically, in the case of light assisted SKPM, measured surface potential voltage represents the change in surface band bending.^[35] SKPM is acquired under dark conditions and UV illumination using an UV-LED emitter at 280 nm. The LPS with $2 \mu\text{m}$ periodicity was used in the characterization. A monotonic contact potential difference (CPD) increase in surface potential from 2.75 nW cm^{-2} , when the LED is turned on, up to flux of $9 \mu\text{W cm}^{-2}$ was observed, saturating for higher values. As shown in Figure 6a–c, CPD holds between 1.8 and 2.0 V under dark condition, whereas it increases up to ≈ 2.3 V, when the above band gap UV illumination is turned on. This is clearly recognizable as a change in the offset on the vertical line-profile of Figure 6a, affecting both the III and N-polar regions and indicating the presence of photogenerated charges all over the sample surface. A closer look at the CPD distribution indicates that the potential of III-polar domains is higher than that of N-polar by 0.1 V under each illumination condition, indicating a charge redistribution between the III and the N-polar domains (see Figure S8 in the Supporting Information). This surface potential difference suggests that surface band bending of the III-polar is larger than that of the N-polar,^[35] promoting the idea that depletion of electrons in the III-polar domains will flow into adjacent N-polar and recombine with holes radiatively. Our experimental SKPM result supports the lateral band diagram shown in Figure 1a, and it is also consistent with previous reports that higher luminescence intensities were observed in the IDBs.^[13,27]

Finally, to provide deeper understanding on the carrier distributions in III-polar, N-polar, and IDB under UV illumination, LPS MQWs were characterized using two additional AFM-related electrical techniques, i.e., electrostatic force microscopy (EFM)^[36] and conductive atomic force microscopy (cAFM)^[34a,37]

as shown in Figure 7. Figure 7a shows the pCEFM amplitude signal, which is proportional to the modulus of electric field unbalance due to the illumination. Positive values indicate a more attractive interaction between the sample and tip (larger values indicate higher concentration of electrons in that region). We distinguished two different behaviors in Figure 7a,b: An average offset on EFM signals (≈ 1.5 – 2 nN in amplitude and 0.5° in phase, visible as yellow-green signal) extending all over the sample surface, indicating a general response of the sample and it is consistent with the results of SKPM. On top of this, several hot spots, depicted as red and blue areas, concentrate mostly in the IDB, suggesting more accumulation of electrons in the vicinity of IDB. The same behavior is confirmed and further highlighted by the pCEFM phase signal (Figure 7b), being more sensitive to the sign of the (photo-) accumulated charges. The different conductivity of the N and III-polar domains comes out clearly shown in Figure 7c, where the schematic image of the setup is illustrated on the left. Dramatic different behaviors between N and III-polar domains are observed: in correspondence of the III-polar domain (green and blue curves) there is neither significant total current nor photocurrent emerging from the noise floor, indicating that both conductance and photoconductance are much lower than the sensitivity of the instrument. In the N-polar domain, there is a clear signal both on the current and in the photocurrent for voltage, between sample and tip ($V_{\text{sample_bias}}$), < -5 V. Figure 7d,e shows the photocurrent and total current signals, respectively, at $V_{\text{sample_bias}} = -10$ V averaged on four different measurements at each point as a color scale on the 3D topography. This demonstrates how both conductivity and photoconductivity are concentrated on the N-polar region but not detectable in the flat top III-polar domains.

The unique behavior of carrier distributions inside the LPS suggests the possibility of selective doping in micrometer scale. Lateral rectification junction or *p-n* diodes can be fabricated through this technique, in which case current flow is perpendicular to the TDs, thus a significantly reduced influence of

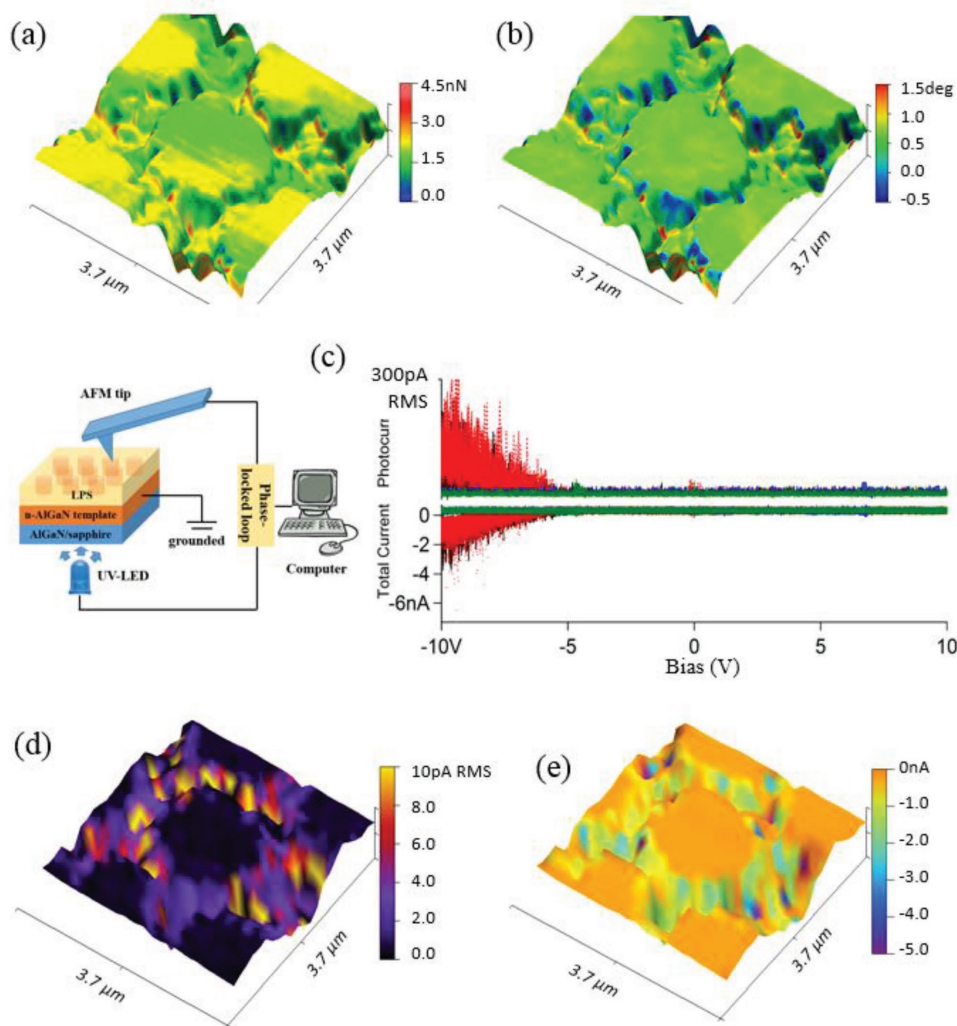


Figure 7. pcEFM signals obtained as subtraction of two EFM images under UV (UV LED flux $3 \mu\text{W cm}^{-2}$) and dark conditions and superimposed as color scale on the 3D rendered topography (image dimensions $3.7 \times 3.7 \mu\text{m}^2$): a) amplitude and b) phase. c) Photocurrent (top) and I_{total} (bottom) versus $V_{\text{sample_bias}}$ acquired ramping voltage between +10 and -10 V. Green and blue curves are for the III-polar domains whereas red and black curves are for the N-polar domains. d) Photocurrent and e) total current signals $V_{\text{sample_bias}} = -10 \text{ V}$ rendered as color scale over 3D topography.

the thin film defects on luminescence efficiency, alleviating the needs for optimization of material quality in AlGaIn and AlN. In addition, with further optimization of the LPS periodicity and the control of defect density at IDB, a balance between optical property and electrical property of LPS-based UV emitters can be obtained, leading to both small carrier diffusion length due to lateral potential variation and efficient carrier injection.

3. Conclusion

Here, we design, fabricate, and characterize a novel AlGaIn/GaN MQW lateral-polarity structure by integrating Al and N-polar domain on a single platform, and realize a significant enhanced luminescence intensity. Enhanced luminescence from the LPS MQW is mainly attributed to surface roughening and compositional inhomogeneities in N-polar domains. We observed that IQE is higher in the N-polar domain and at the IDB in the LPS,

in accordance with the higher luminescence intensity in those regions. The optimized MQW structure design also provides guidance on realizing high wavefunction overlap for efficient emitters. The present findings emphasize the importance of nanoscale polarity control in tuning structural and optical properties of AlGaIn MQWs, which paves the way for next-generation high efficiency UV light sources.

4. Experimental Section

Sample Preparation: 20 nm AlN buffer layers were grown on 2 in. sapphire substrates via AMEC Prismo D-Blue MOCVD reactor at 800°C . Buffer patterning was achieved through PS sphere coating followed by RIE. PS spheres with different diameters (2 and $6 \mu\text{m}$) were synthesized by emulsifier-free emulsion polymerization.^[38] Self-assembled PS spheres on top of AlGaIn MQW structures were formed via a large-area micropropulsive injection method. The spheres were injected into water to form a Langmuir–Blodgett film in a hexagonal configuration

at the air/water interface. Closely packed PS monolayer was transferred to the sapphire substrate with an LT-AlN buffer. Details on the AlGaIn thin film preparation were described elsewhere.^[39] The diameter of PS sphere was then reduced by O₂ trimming, without changing the location of the spheres. RIE times are 20 min for 2 μ m PS and 60 min for 6 μ m PS, respectively. Subsequently, the exposed LT-AlN buffer in between PS spheres was etched by RIE using a mixture of Cl₂ and BCl₃ gases, while the AlN buffer beneath PS spheres remains intact. After a thorough cleaning step, the patterned AlN buffer substrate was re-loaded into the MOCVD chamber for the epitaxial growth. Before epitaxial growth, the patterned buffer first went through a nitridation step under 1100 °C for 5 min. Trimethylaluminum, triethylgallium and ammonia (NH₃) were used as precursors of Al, Ga, and N, respectively. Hydrogen (H₂) was used as the carrier gas. Prior to high-temperature epitaxial growth, patterned AlN buffers were annealed in H₂ for 10 min at 1100 °C and NH₃ for 5 min at 1000 °C in order to heal the RIE damage on sapphire substrate surface. On the top of patterned AlN buffer, 1 μ m AlN thin film was grown at temperature of 1250 °C, followed by 400 nm thick composition graded Al_xGa_{1-x}N template with Al composition decreasing from 50% to 20% in order to gradually release strains induced by lattice mismatch. After 600 nm thick n-Al_{0.2}Ga_{0.8}N growth, ten pairs of Al_{0.1}Ga_{0.9}N-GaN MQWs were deposited at 1100 °C, acting as light emitting region.

Characterization: Surface morphologies of MQW structures were characterized by Olympus optical microscopy, Veeco Dimension 3100 V AFM, and Hitachi S-4800 SEM. Room temperature PL studies were performed using an Ar-F (193 nm) excimer laser at pumping power of 50 mW cm⁻², collected by a Horiba iHR550 spectrometer. PL mapping was performed via a Renishaw PL spectroscopy with a μ -PL setup. The TEM samples were prepared using an FEI Helios dual-beam focused ion beam scanning electron microscope system with a Ga ion source. Cross-sectional morphology of both polarity domains, MQW layer thickness, as well as dislocation distribution were characterized by an HAADF-STEM using an FEI probe-corrected Titan microscope operated at an acceleration voltage of 300 kV. For the photoelectrical AFM measurement an MFP3Dbo AFM (Oxford Instruments Asylum Research, Santa Barbara, CA) mounted on an inverted optical microscope Nikon Ti-S was used. Ti/Ir-coated silicon tip (Asylum Electreliver, spring constant 2.95 N m⁻¹) was used in the SKPM measurement. For pCEFM Ti/Ir-coated silicon tip was used (Asylum Electreliver, spring constant 2.95 N m⁻¹), EFM amplitude \approx 0.5 free oscillation amplitude, NAP height 50 nm, Tip bias between -3 V and = 3 V (0.5 V steps) both under UV illumination (4.9 μ W cm⁻²) and dark condition on the same area. pCEFM amplitude and phase were obtained by subtracting the relative EFM amplitude and phase images at each tip voltage, after evaluating the drift by means of cross correlation on topography. For pCAFM a conductive AFM module (dual orca G₀ = 10⁶ V A⁻¹, G₁ = 10⁹ V A⁻¹) and Ti/Ir conductive tips (Asylum Research, nominal spring constant = 2 N m⁻¹) were used. I/V (triangular V bias signal, range \pm 10 V) spectroscopy maps were acquired while UV LED was modulated ON/OFF (modulation: TTL, f = 1.211 kHz), amplified on G₀, bandpass filtered (first-order Bessel band pass filter centered at the same frequency and two decades wide (two stage SR SIM 965)), synchronously detected by a lock-in amplifier (Stanford Research SR830, T = 10 ms, sensitivity = 100 mV), and acquired in parallel to the current signal. An R = 1 G-ohm resistor was placed in series to the sample to limit the maximum current through the tip.

Supporting Information

Supporting Information is available from the Wiley Online Library or from the author.

Acknowledgements

W.G. and H.S. contributed equally to this work. The NIMTE authors acknowledge the support of the National Key Research and Development

Program of China (Grant No. 2016YFB0400802), the National Natural Science Foundation of China (Grant No. 61704176), and the Open project of Zhejiang Key Laboratory for Advanced Microelectronic Intelligent Systems and Applications (Grant No. ZJUAMIS1704). The KAUST authors acknowledge the support of the KAUST Baseline BAS/1/1664-01-01, OCRF-2014-CRG3-6214038, and the National Natural Science Foundation of China (Grant No. 61774065). The authors greatly appreciate the help from Prof. Zi-hui Zhang and co-workers of Hebei University of Technology in theoretical band diagram calculations and fruitful discussions on device physics.

Conflict of Interest

The authors declare no conflict of interest.

Keywords

inversion domain boundaries (IDBs), lateral-polarity structures (LPSs), luminescence intensity, multiple quantum wells, ultraviolet light

Received: April 8, 2018

Revised: May 7, 2018

Published online: June 8, 2018

- [1] a) T. Takano, T. Mino, J. Sakai, N. Noguchi, K. Tsubaki, H. Hirayama, *Appl. Phys. Express* **2017**, *10*, 031002; b) M. A. Wuertele, T. Kolbe, M. Lipsz, A. Kuelberg, M. Weyers, M. Kneissl, M. Jekel, *Water Res.* **2011**, *45*, 1481.
- [2] K. J. Dabing Li, X. Sun, C. Guo, *Adv. Opt. Photonics* **2018**, *10*, 43.
- [3] a) Y. Taniyasu, M. Kasu, T. Makimoto, *Nature* **2006**, *441*, 325; b) Z. Bryan, I. Bryan, J. Xie, S. Mita, Z. Sitar, R. Collazo, *Appl. Phys. Lett.* **2015**, *106*, 325; c) M. Kneissl, T. Kolbe, C. Chua, V. Kueller, N. Lobo, J. Stellmach, A. Knauer, H. Rodriguez, S. Einfeldt, Z. Yang, *Semicond. Sci. Technol.* **2010**, *26*, 014036.
- [4] a) Y. Narukawa, M. Ichikawa, D. Sanga, M. Sano, T. Mukai, *J. Phys. D: Appl. Phys.* **2010**, *43*, 354002; b) H. Morkoç, S. N. Mohammad, *Science* **1995**, *267*, 51.
- [5] C. Li, H. Wang, H. Liu, S. J. Chua, *J. Vac. Sci. Technol., A* **2016**, *34*, 051501.
- [6] S. Keller, H. Li, M. Laurent, Y. Hu, N. Pfaff, J. Lu, D. F. Brown, N. A. Fichtenbaum, J. S. Speck, S. P. DenBaars, U. K. Mishra, *Semicond. Sci. Technol.* **2014**, *29*, 113001.
- [7] W. Guo, R. Kirste, I. Bryan, Z. Bryan, L. Hussey, P. Reddy, J. Tweedie, R. Collazo, Z. Sitar, *Appl. Phys. Lett.* **2015**, *106*, 1594.
- [8] a) M. Belloeil, B. Gayral, B. Daudin, *Nano Lett.* **2016**, *16*, 960; b) P. Wang, X. Wang, T. Wang, C. S. Tan, B. Sheng, X. Sun, M. Li, X. Rong, X. Zheng, Z. Chen, *Adv. Funct. Mater.* **2017**, *27*, 1604854.
- [9] a) R. Kirste, S. Mita, L. Hussey, M. P. Hoffmann, W. Guo, I. Bryan, Z. Bryan, J. Tweedie, J. Xie, M. Gerhold, *Appl. Phys. Lett.* **2013**, *102*, 181913; b) D. Alden, W. Guo, R. Kirste, F. Kaess, I. Bryan, T. Troha, A. Bagal, P. Reddy, L. H. Hernandezbalderrama, A. Franke, *Appl. Phys. Lett.* **2016**, *108*, 222101; c) M. P. Hoffmann, R. Kirste, S. Mita, W. Guo, J. Tweedie, M. Bobea, I. Bryan, Z. Bryan, M. Gerhold, R. Collazo, *Phys. Status Solidi A* **2015**, *212*, 1039; d) J. Hite, *J. Cryst. Growth* **2016**, *456*, 133.
- [10] A. Chowdhury, H. M. Ng, M. Bhardwaj, N. G. Weimann, *Appl. Phys. Lett.* **2003**, *83*, 1077.
- [11] R. Collazo, S. Mita, J. Xie, A. Rice, J. Tweedie, R. Dalmau, Z. Sitar, *Phys. Status Solidi* **2010**, *207*, 45.
- [12] S. Mita, R. Collazo, Z. Sitar, *J. Cryst. Growth* **2009**, *311*, 3044.

- [13] R. Kirste, R. Collazo, G. Callsen, M. R. Wagner, T. Kure, J. Sebastian Reparaz, S. Mita, J. Xie, A. Rice, J. Tweedie, *J. Appl. Phys.* **2011**, 110, 093503.
- [14] P. M. Coulon, M. Mexis, M. Teisseire, M. Jublot, P. Venegues, M. Leroux, J. Zuniga-Perez, *J. Appl. Phys.* **2014**, 115, 3228.
- [15] a) V. Fiorentini, *Appl. Phys. Lett.* **2003**, 82, 1182; b) W. C. Yang, B. J. Rodriguez, M. Park, R. J. Nemanich, O. Ambacher, V. Cimalla, *J. Appl. Phys.* **2003**, 94, 5720.
- [16] P. Reddy, I. Bryan, Z. Bryan, W. Guo, L. Hussey, R. Collazo, Z. Sitar, *J. Appl. Phys.* **2014**, 116, 202101.
- [17] R. Collazo, S. Mita, A. Rice, R. F. Dalmau, *Appl. Phys. Lett.* **2007**, 91, 212103.
- [18] W.-C. Yang, B. J. Rodriguez, M. Park, R. Nemanich, O. Ambacher, V. Cimalla, *J. Appl. Phys.* **2003**, 94, 5720.
- [19] B. J. Rodriguez, W. C. Yang, R. J. Nemanich, A. Gruverman, *Appl. Phys. Lett.* **2005**, 86, 3522.
- [20] A. Aleksov, R. Collazo, S. Mita, R. Schlessler, Z. Sitar, *Appl. Phys. Lett.* **2006**, 89, 355.
- [21] Y. Li, R. Zhang, B. Liu, Z. Xie, G. Zhang, T. Tao, Z. Zhuang, T. Zhi, Y. Zheng, *J. Appl. Phys.* **2014**, 116, 945.
- [22] Y. N. Ahn, S. H. Lee, S. K. Lim, K. J. Woo, H. Kim, *Mater. Sci. Eng.: B* **2015**, 193, 105.
- [23] S. Schlichting, G. M. O. Hönig, J. Müßener, P. Hille, T. Grieb, J. Teubert, J. Schörmann, M. R. Wagner, A. Rosenauer, M. Eickhoff, A. Hoffmann, Tuning of the Quantum-Confined Stark Effect in Wurtzite [0001] Group-III-Nitride Nanostructures by the Internal-Field-Guarded-Active-Region Design, arXiv:1707.06882, **2017**.
- [24] C. H. Kuo, Y. K. Fu, L. C. Chang, Y. A. Chen, *IEEE J. Quantum Electron.* **2014**, 50, 255.
- [25] a) E. Francesco Pecora, W. Zhang, A. Yu. Nikiforov, L. Zhou, D. J. Smith, J. Yin, R. Paiella, L. Dal Negro, T. Moustakas, *Appl. Phys. Lett.* **2012**, 100, 061111; b) Y. Liao, C. Thomidis, C. K. Kao, T. D. Moustakas, *Appl. Phys. Lett.* **2011**, 98, 77.
- [26] R. R. Pelá, C. Caetano, M. Marques, L. G. Ferreira, J. Furthmüller, L. K. Teles, *Appl. Phys. Lett.* **2011**, 98, 8.
- [27] P. J. Schuck, M. D. Mason, R. D. Grober, O. Ambacher, A. P. Lima, C. Miskys, R. Dimitrov, M. Stutzmann, *Appl. Phys. Lett.* **2001**, 79, 952.
- [28] M. Funato, S. Ichikawa, K. Kumamoto, Y. Kawakami, presented at *SPIE OPTO*, San Francisco, California, USA, February **2017**.
- [29] H. Hirayama, N. Noguchi, S. Fujikawa, J. Norimatsu, N. Kamata, T. Takano, K. Tsubaki, in *Gallium Nitride Materials and Devices IV*, Vol. 7216 (Eds: H. Morkoc, C. W. Litton, J. I. Chyi, Y. Nanishi, J. Piprek, E. Yoon), International Society for Optics and Photonics **2009**, p. 721621.
- [30] J. Mickevičius, G. Tamulaitis, M. Shur, M. Shatalov, J. Yang, R. Gaska, *Appl. Phys. Lett.* **2012**, 101, 211902.
- [31] B. Pantha, R. Dahal, M. Nakarmi, N. Nepal, J. Li, J. Lin, H. Jiang, Q. Paduano, D. Weyburne, *Appl. Phys. Lett.* **2007**, 90, 241101.
- [32] P. Dong, J. Yan, J. Wang, Y. Zhang, C. Geng, T. Wei, P. Cong, Y. Zhang, J. Zeng, Y. Tian, *Appl. Phys. Lett.* **2013**, 102, 12.
- [33] a) C. E. Dreyer, A. Janotti, C. G. Van de Walle, D. Vanderbilt, *Phys. Rev. X* **2016**, 6, 021038; b) Y.-A. Chang, F.-M. Chen, S.-R. Li, Y.-K. Kuo, *IEEE Trans. Electron Devices* **2014**, 61, 3233.
- [34] a) L. S. Pingree, O. G. Reid, D. S. Ginger, *Adv. Mater.* **2009**, 21, 19; b) H. Hoppe, T. Glatzel, M. Niggemann, A. Hinsch, M. C. Lux-Steiner, N. Sariciftci, *Nano Lett.* **2005**, 5, 269; c) K. Maturova, M. Kemerink, M. M. Wienk, D. S. Charrier, R. A. Janssen, *Adv. Funct. Mater.* **2009**, 19, 1379.
- [35] J. Wei, R. Neumann, X. Wang, S. Li, S. Fündling, S. Merzsch, M. A. Al-Suleiman, Ü. Sökmén, H. H. Wehmann, A. Waag, *Phys. Status Solidi C* **2011**, 8, 2157.
- [36] D. C. Coffey, D. S. Ginger, *Nat. Mater.* **2006**, 5, 735.
- [37] M. J. Romero, A. J. Morfa, T. H. Reilly, D. L. J. Van, M. Al-Jassim, *Nano Lett.* **2009**, 9, 3904.
- [38] P. Gao, J. He, S. Zhou, X. Yang, S. Li, S. Jiang, D. Wang, T. Yu, J. Ye, Y. Cui, *Nano Lett.* **2015**, 15, 4591.
- [39] P. Dong, J. Yan, Y. Zhang, J. Wang, J. Zeng, C. Geng, P. Cong, L. Sun, T. Wei, L. Zhao, *J. Cryst. Growth* **2014**, 395, 9.